Unified predictive flux control
for EESM, IM, PMSM and SyRM

Johannes Stoß 🆔
Elektrotechnisches Institut (ETI)
Karlsruhe Institute of Technology (KIT)
Karlsruhe, Germany
johannes.stoss@kit.edu

Leonard Geier
Elektrotechnisches Institut (ETI)
Karlsruhe Institute of Technology (KIT)
Karlsruhe, Germany
leonard.geier@kit.edu

Akif Karayel
Elektrotechnisches Institut (ETI)
Karlsruhe Institute of Technology (KIT)
Karlsruhe, Germany

Simon Decker
Elektrotechnisches Institut (ETI)
Karlsruhe Institute of Technology (KIT)
Karlsruhe, Germany
🆔 0000-0001-8185-2309

Andreas Liske 🆔
Elektrotechnisches Institut (ETI)
Karlsruhe Institute of Technology (KIT)
Karlsruhe, Germany
andreas.liske@kit.edu

Marc Hiller
Elektrotechnisches Institut (ETI)
Karlsruhe Institute of Technology (KIT)
Karlsruhe, Germany
marc.hiller@kit.edu

Abstract— **This paper describes a new method for a high dynamic and nonlinear unified model predictive control of induction motors (IM), permanent magnet synchronous machines (PMSM), synchronous reluctance machines (SyRM) and electrically excited synchronous machines (EESM) using the same control algorithm. This is enabled by a unified nonlinear machine model that allows the described machines to be modelled and controlled basically as a variation of the EESM. This allows simple and fast adaptation of drive systems to new motors as only the model parameters of the control system need to be adjusted. By eliminating the need to customize the code base for individual machine types, software platforms can be simplified to handle even large product ranges cost-effectively.**

Keywords— Electrically Excited Synchronous Machine, Induction Motor, Synchronous motor, Permanent magnet motor, Synchronous Reluctance Machine, Flux Model, MPC (Model-based Predictive Control), Non-linear control

I. Introduction

Technology is being modularized increasingly to allow efficient adaption to individual requirements. To enable a quick replacement of machine types with identical drive inverters, signal processing and control, this paper presents a new model predictive flux control method which controls different machine types with an identical code base and modelling. The benefit of this method is that implementation and testing of the control algorithm must be carried out just once. Afterwards, only the individual data set for the connected machine must be loaded. This has no effect on the quality and dynamics of the controller as well as the real-time capability of the system itself. As the code base is identical for all shown machine types, significant reduction the software maintenance effort for a large product range can be achieved compared to a specifically adapted solution. This allows system modifications to be carried out fast and easy and therefore cost-effective while maintaining high control dynamics and accuracy.

II. Unified Machine Model

In this chapter the modelling approach is outlined. It is based on the assumption that all machines consist of three symmetrical phases, which are star connected. Furthermore, frequency and angle dependences of flux linkages, resistances, iron losses and other parasitic effects are neglected.

The modelling is driven by the fact, that all important machine characteristics can be described by flux linkages of the stator and rotor in dependence of the associated currents. This implicitly includes all coupling factors of the IM and EESM between the different winding systems in stator and rotor. Since the machine types differ only due to their rotor design, the stator voltage equations are identical for all machines. Thereby, the synchronous machines are modelled in rotor-orientation and the IM in rotor flux-orientation. The stator voltage equations are given with ω_S being the electrical stator frequency, R_S the stator resistance, ψ_{Sd} and ψ_{Sq} the stator flux linkages and i_{Sd}, i_{Sq} the stator currents in the rotating dq reference frame.

$$v_{Sd} = R_S\, i_{Sd} + \dot{\psi}_{Sd} - \omega_S \psi_{Sq} \tag{1}$$

$$v_{Sq} = R_S\, i_{Sq} + \dot{\psi}_{Sq} + \omega_S \psi_{Sd} \tag{2}$$

The inner torque T_i is calculated identically for all machines using the stator flux linkages and currents [1–3].

$$T_i = \frac{3}{2} \cdot p \cdot (\psi_{Sd} \cdot i_{Sq} - \psi_{Sq} \cdot i_{Sd}) \tag{3}$$

Stator and rotor are coupled via the respective flux linkage. They only differ due to the leakage flux, which is typically small compared to the d-flux in stator or rotor. The modeling for the different rotors is described in detail below.

A. Electrically Excited Synchronous Machines

With the additional voltage source v_{Rd} that supplies the rotor current i_{Rd}, the EESM is the most complex system and therefore the initial point for the model description. As shown below, the rotor voltage equations of the shown machine types can be described as a variation of the EESM. The EESM rotor voltage equation is given with R_R being the rotor resistance.

$$v_{Rd} = R_R \cdot i_{Rd} + \dot{\psi}_{Rd} \tag{4}$$

In the d-axis of the rotor, the current in the excitation winding can be changed by applying a voltage which results in a change of the rotor flux ψ_{Rd}. The stator and rotor flux are modeled in dependence of i_{Sd}, i_{Sq} and i_{Rd}, resulting in:

$$f_{\psi_{EESM}}: \mathbb{R}^3 \to \mathbb{R}^3, (i_{Sd}, i_{Sq}, i_{Rd}) \to (\psi_{Sd}, \psi_{Sq}, \psi_{Rd}) \tag{5}$$
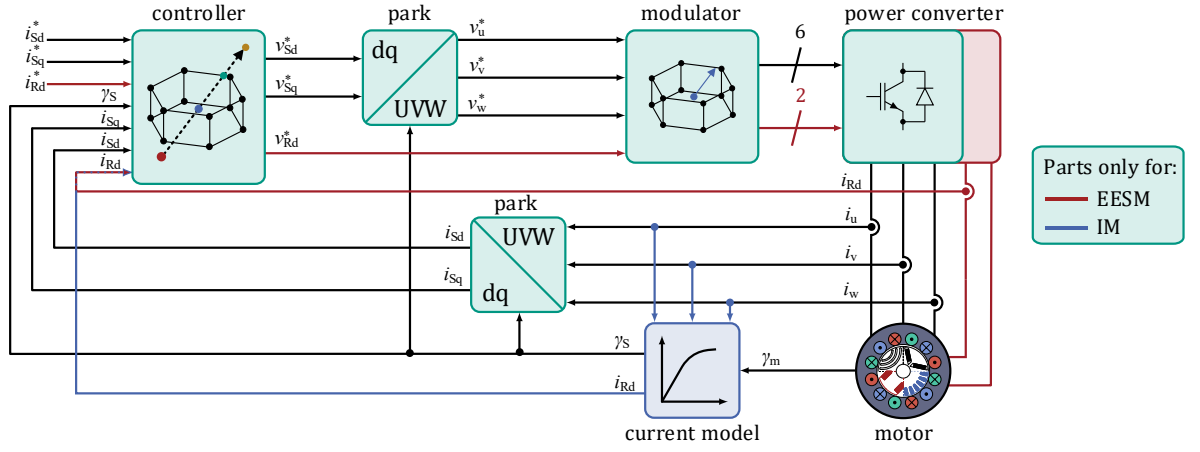
Fig. 1. Block diagram of the generalized control system.

B. Permanent Magnet Synchronous Machines

The rotor flux of the PMSM behaves as an EESM rotor with an arbitrary constant excitation current $k > 0$. As the rotor flux cannot be measured or changed by an additional rotor circuit, no rotor voltage equation is necessary. Therefore, the flux linkages are a two-dimensional function:

$$f_{\psi \text{PMSM}}: \mathbb{R}^2 \to \mathbb{R}^2, \left(i_{\text{Sd}}, i_{\text{Sq}}, i_{\text{Rd}} = k\right) \to \left(\psi_{\text{Sd}}, \psi_{\text{Sq}}\right) \quad (6)$$

C. Synchronous Reluctance Machines

Due to the lack of permanent magnets, the SyRM rotor has no permanent excitation and can thus be modelled as an EESM rotor without rotor current. This also results in a two-dimensional function for the flux linkages:

$$f_{\psi \text{SyRM}}: \mathbb{R}^2 \to \mathbb{R}^2, \left(i_{\text{Sd}}, i_{\text{Sq}}, i_{\text{Rd}} = 0\right) \to \left(\psi_{\text{Sd}}, \psi_{\text{Sq}}\right) \quad (7)$$

D. Induction Motor

In case of the IM, the bars of the squirrel-cage are short-circuited, therefore the rotor voltage is always zero. The rotor current is caused by the coupling between stator and rotor. Consequently it can only be influenced indirectly. The induction motor is modeled in rotor flux orientation, meaning $\psi_{\text{Rq}} = 0$. ψ_{Rq} is therefore not included in the rotor voltage equations.

$$v_{\text{Rd}} = 0 = R_{\text{R}} \cdot i_{\text{Rd}} + \dot{\psi}_{\text{Rd}} \quad (8)$$

$$v_{\text{Rq}} = 0 = R_{\text{R}} \cdot i_{\text{Rq}} + \psi_{\text{Rd}} \cdot \omega_{\text{R}} \quad (9)$$

With ω_{R} being the rotor angular frequency, which is defined by the stator frequency and the slip s at the current operating point.

$$\omega_{\text{R}} = \omega_{\text{S}} \cdot s \quad (10)$$

As the flux linkages depend on the rotor current in transient operation, they are given also as a function of the rotor current.

$$f_{\psi \text{IM}}: \mathbb{R}^3 \to \mathbb{R}^3, \left(i_{\text{Sd}}, i_{\text{Sq}}, i_{\text{Rd}}\right) \to \left(\psi_{\text{Sd}}, \psi_{\text{Sq}}, \psi_{\text{Rd}}\right) \quad (11)$$

A challenge of this approach is that the rotor currents of the IM can usually not be measured but are necessary to determine the present state of the system. In this paper, the nonlinear current model of [4] is used. Its operating principle is outlined in section III D.

III. CONTROL STRUCTURE

The presented control method (fig. 1) is based on a control algorithm for PMSM [5] and EESM [6]. It was enhanced and generalized to allow operation of all four machine types using the same code base.

For operation, the following machine parameters are necessary:

- number of pole pairs p

- resistance of rotor R_{R} and stator windings R_{S}

- flux maps: $\vec{\psi}: \vec{\imath} \to \vec{\psi}$

- inverse flux maps: $\vec{\psi}^{-1}: \vec{\psi} \to \vec{\imath}$

- voltage and current limits of the machine and inverter (lower limit applies at each operating point)

- controller time $T_C = 1/f_c$ (f_c equals controller frequency)

- parameters of the current model for IM operation

using $\vec{\psi} = \left[\psi_{\text{Sd}}, \psi_{\text{Sq}}, \psi_{\text{Rd}}\right]$ and $\vec{\imath} = \left[i_{\text{Sd}}, i_{\text{Sq}}, i_{\text{Rd}}\right]$.

The flux maps $\vec{\psi}: \vec{\imath} \to \vec{\psi}$ allow modelling of the behavior of all machines (EESM, IM, PMSM, SyRM) with the influence of iron saturation. They can be determined either from a measurement or FEA simulation [3, 4, 7–9]. To represent the influence of other parameters, like temperature and speed, the data set can be extended to include the additional dimensions. The inversion of the flux maps was performed according to [10].

The control structure in fig. 1 consists of all parts which are necessary to allow universal machine operation. The controller, modulator and park transformation (fig. 1 – green) are thereby identical for the four machine types. Individual adaptation is not required.

The additional winding system in the EESM requires an extension of the power converter by a half or full bridge circuit and a current measurement (fig. 1 – red). Since the transformation angle for the rotor flux orientation is not measurable directly at IM operation, the nonlinear current model needs to be added (blue).

Fig. 2 gives an overview of the universal controller. As input variables, the measured currents and angle values are required. The set currents serve as target values. The current

setpoint is converted into flux linkages representing the stationary operating point in flux domain. This implies for IM operation that the set stator currents have to be reached with the rotor current being completely decayed and the rotor flux being constant in order to meet the set value.

Due to the usage of (inverse) flux maps, all system parameters in the current and flux domain are known at any time. The implementation of the control strategy is performed in the flux domain, while the interfaces are in current domain due to the availability of sensor signals. By expressing the control problem in flux domain, it is greatly simplified and thus can be solved more efficiently, as the non-linearities of the system are only reflected in the mapping of the flux linkages to the currents.
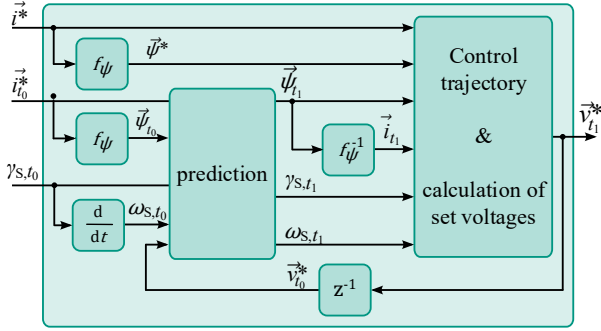

Fig. 2. Block diagram of the controller.

The operation of the controller is illustrated using the time sequence in Fig. 3. The measurements are taken at time t_0. Using the flux maps, the current measurements allow determination of the flux linkages at t_0. As the new nominal voltages can only be set after the calculation interval $[t_0, t_1]$, the currents and flux linkages at the time t_1 must be estimated first. This is achieved by the prediction block, which is explained in section A.
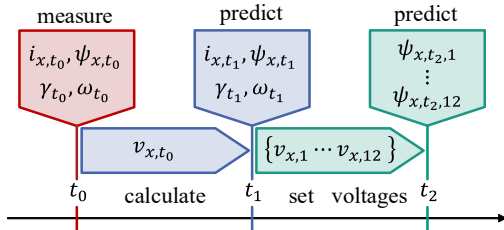

Fig. 3. Time sequence of the control algorithm.

The knowledge of the state variables at the beginning of the new control interval enables calculation of the output voltages for the next control interval $[t_1, t_2]$. Therefore, the target trajectory is evaluated first followed by the calculation of the new output voltages. The procedure is explained in section B and C.

A. Prediction

The discretized voltage equations allow prediction of the flux linkage at t_1 utilizing the set voltage from the previous control interval $\vec{v}_{t_0}^*$ and the related current and angle measurements [6].

$$\psi_{\mathrm{Sd},t_n} = \psi_{\mathrm{Sd},t_{n-1}} +$$

$$\frac{v_{\mathrm{Sd},t_{n-1}} - R_S \cdot i_{\mathrm{Sd},t_{n-1}} + \omega_S \cdot \psi_{\mathrm{Sq},t_{n-1}}}{1 + \frac{1}{4}\omega_S^2 \cdot T_C^2} \cdot T_C +$$

$$\frac{v_{\mathrm{Sq},t_{n-1}} - R_S \cdot i_{\mathrm{Sq},t_{n-1}} - \omega_S \cdot \psi_{\mathrm{Sd},t_{n-1}}}{1 + \frac{1}{4}\omega_S^2 \cdot T_C^2} \cdot \frac{\omega_S \cdot T_C^2}{2} \tag{12}$$

$$\psi_{\mathrm{Sq},t_n} = \psi_{\mathrm{Sq},t_{n-1}} + \tag{13}$$

$$\frac{v_{\mathrm{Sq},t_{n-1}} - R_S \cdot i_{\mathrm{Sq},t_{n-1}} - \omega_S \cdot \psi_{\mathrm{Sd},t_{n-1}}}{1 + \frac{1}{4}\omega_S^2 \cdot T^2} \cdot T_C +$$

$$\frac{-v_{\mathrm{Sd},t_{n-1}} + R_S \cdot i_{\mathrm{Sd},t_{n-1}} - \omega_S \cdot \psi_{\mathrm{Sq},t_{n-1}}}{1 + \frac{1}{4}\omega_S^2 \cdot T_C^2} \cdot \frac{\omega_S \cdot T_C^2}{2}$$

$$\psi_{\mathrm{Rd},t_n} = \psi_{\mathrm{Rd},t_{n-1}} + \tag{14}$$

$$(v_{\mathrm{Rd},t_{n-1}} - R_R \cdot i_{\mathrm{Rd},t_{n-1}}) \cdot T_C$$

The angular velocity ω_S is thereby assumed to be constant during the interval $[t_0, t_2]$. After calculating $\vec{\psi}_{t_1}$, the currents at t_1 are determined by the inverse flux maps. The angle γ_{t_1} at the next control interval is predicted using ω_S.

$$\gamma_{t_1} = \gamma_{t_0} + \omega_S \cdot T_C \tag{15}$$

To enable the calculation of the target voltage, the target flux linkage for the next interval must be calculated first.
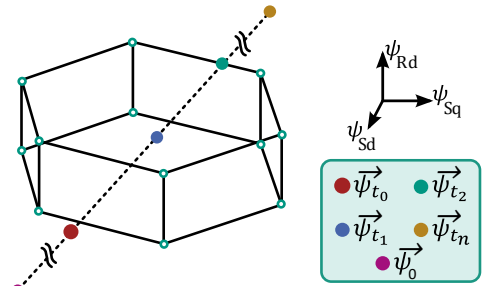
B. Control Trajectory

Fig. 4. Flux trajectory and prediction horizon as 3D hexagon prism for EESM operation.

To get from the operating point before the setpoint change, represented by $\vec{\psi}_0$, to the new desired operating point $\vec{\psi}_{t_n}$ at t_n, a straight line is used as control trajectory since it represents the shortest connection between two points in the flux domain. As the length of the trajectory in the respective spatial axis in the flux domain corresponds to the applied voltage-time area, neglecting the ohmic voltage drop, this represents the most dynamic trajectory for the system at standstill.

For increased control performance especially at high rotational speed, other objective functions can be applied, but will require additional computation time. Possible implementations for PMSM and SyRM are shown in [5].

$$G_\psi(r) = \vec{\psi}_0 + (\vec{\psi}_{t_n} - \vec{\psi}_0) \cdot r, \qquad r \in [0,1] \tag{16}$$

The trajectory is thereby defined by the state variables at occurrence of the setpoint step $\vec{\psi}_0$ and the new target value $\vec{\psi}_{t_n}$ (fig. 4). No adaption of the trajectory during transient operation is performed to minimize distortion caused by model errors.

C. Calculation of set voltages

Using the voltage vectors for all switching states of the 3-phase 2-level stator- and the rotor power converter, the maximum achievable flux points (boundary of prediction horizon – fig. 4) for the next control interval can be determined starting from $\vec{\psi}_{t_1}$ in fig. 4. For the IM, PMSM and SyRM, the six active switching states of the 2-level stator inverter lead to a 2D hexagon prediction horizon. The additional rotor voltage that can be applied at the EESM, results in the 3D hexagon prism as shown in fig. 4.

By calculating the intersection point between the control trajectory (fig. 4 – dotted line) and the prediction horizon, the optimal flux setpoint for the next control interval is chosen. Since at IM operation the prediction horizon is only 2D while the set trajectory is a 3D function, the set trajectory in the flux domain is executed as a projection of the set trajectory on the d- and q-dimensions. This can lead to deviations of the rotor flux ψ_{Rd}.

To ensure that the current limits are met, the flux linkage point $\vec{\psi}_{t_2}$ is transformed into the current domain using the inverse flux maps. If the current limit is exceeded, the step size is reduced to the current limit. If the limits are maintained, no modification is made. Afterwards, the current point is transformed back into the flux domain. In the final step, the target voltage for the next control interval is calculated using the discretized voltage equations and the modified target flux.

$$v_{\mathrm{Sd},t_1}^* = R_{\mathrm{S}}\frac{\left(i_{\mathrm{Sd},t_1} + i_{\mathrm{Sd},t_2}^*\right)}{2} + \frac{\left(\psi_{\mathrm{Sd},t_2}^* - \psi_{\mathrm{Sd},t_1}\right)}{T_{\mathrm{C}}} - \frac{\omega_{\mathrm{S}}\left(\psi_{\mathrm{Sq},t_1} + \psi_{\mathrm{Sq},t_2}^*\right)}{2} \tag{17}$$

$$v_{\mathrm{Sq},t_1}^* = R_{\mathrm{S}}\frac{\left(i_{\mathrm{Sq},t_1} + i_{\mathrm{Sq},t_2}^*\right)}{2} + \frac{\left(\psi_{\mathrm{Sq},t_2}^* - \psi_{\mathrm{Sq},t_1}\right)}{T_{\mathrm{C}}} + \frac{\omega_{\mathrm{S}}\left(\psi_{\mathrm{Sd},t_1} + \psi_{\mathrm{Sd},t_2}^*\right)}{2} \tag{18}$$

$$v_{\mathrm{Rd},t_1}^* = R_{\mathrm{R}}\frac{\left(i_{\mathrm{Rd},t_1} + i_{\mathrm{Rd},t_2}^*\right)}{2} + \frac{\left(\psi_{\mathrm{Rd},t_2}^* - \psi_{\mathrm{Rd},t_1}\right)}{T_{\mathrm{C}}} \tag{19}$$

Based on this, the optimal combination of switching states for the rotor and stator power converter are selected by the modulator.

D. Estimation of the rotor current

The presented algorithm is carried out in rotor or rotor flux orientation. Since the transformation angle can only be determined directly by the encoder for synchronous machines, the nonlinear current model shown in [4] is additionally used in case of the induction motor. To further allow rotor current estimation, the current model is extended based on the rotor flux equation.

The rotor flux is therefore estimated using the transformer equivalent circuit diagram, neglecting cross coupling, with L_{m} being the mutual and $L_{\mathrm{R}\sigma}$ the rotor stray inductance of the IM:

$$\psi_{\mathrm{Rd}} = (L_{\mathrm{m}} + L_{\mathrm{R}\sigma}) \cdot i_{\mathrm{Rd}} + L_{\mathrm{m}} \cdot i_{\mathrm{Sd}} \tag{20}$$

This allows estimation of the rotor current:

$$i_{\mathrm{Rd}} = \frac{\psi_{\mathrm{Rd}} - L_{\mathrm{m}} \cdot i_{\mathrm{Sd}}}{L_{\mathrm{m}} + L_{\mathrm{R}\sigma}} \tag{21}$$

Thereby, the stray inductance is assumed to be constant, while the mutual inductance is modelled in this paper as a function of the rotor flux linkage.

$$f\colon \mathbb{R} \to \mathbb{R}, \psi_{\mathrm{Rd}} \to L_{\mathrm{m}} \tag{22}$$

IV. SIMULATION RESULTS

Since nonlinear DUTs were not available for all machine types at the time of publication, the results for the SyRM and PMSM operation are demonstrated through simulation, while demonstrations of the control algorithm for IM and EESM operation are given by measurements in chapter V.

The Simulations were performed by the *ETI Model drive train* in *MATLAB®*, which allows an acausal simulation of the machines in *MATLAB Simscape®* using the machine flux linkage maps [11]. All simulations are performed at 8 kHz controller and switching frequency.
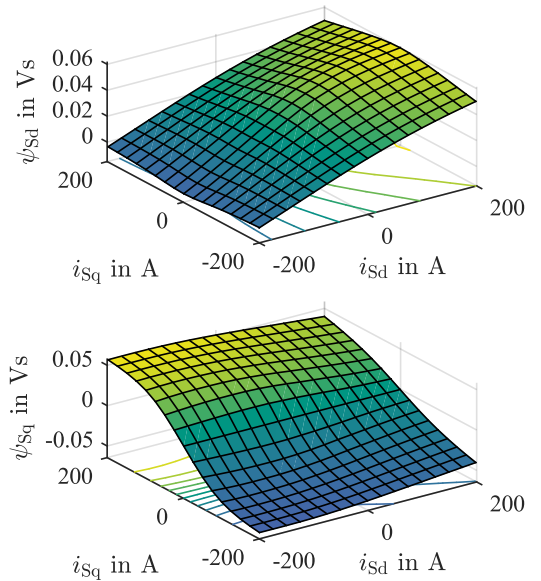
A. Permanent magnet synchronus machine

Fig. 5. Maps of the Sd- and Sq-flux linkage of the *ETI-S01-30-20*.

For PMSM operation the *ETI-S01-30-20* dataset is used for the simulation [12]. The characteristics are given in Table I. The PMSM is fully characterized by its flux maps, which have been generated by finite element simulation and verified by measurements. The flux maps are shown in fig. 5. Saturation and cross coupling is clearly visible.

A simulated setpoint step at 5000 rpm can be seen at fig. 6. The setpoint current was chosen to $i_{\mathrm{Sd}} = -125$ A and $i_{\mathrm{Sq}} = 150$ A . Fig. 6 a) shows the current response. After the setpoint step at 0 ms, a dead time of one control interval for the calculation of the new output voltages is visible. Afterwards, the controller reaches the new setpoint within 0.5 ms, which corresponds to 4 controller intervals.

TABLE I. PMSM MACHINE DATA [12]

Symbol	Meaning	value
p	Number of polepairs	3
$i_{\text{cont.}}$	Continuous rms stator current	100 A
v_{DC}	DC link voltage	400 V
$P_{\text{cont.}}$	Continuous Power	30 kW
R_{S}	Stator resistance	44 mΩ

The output voltages are shown in fig 6 b). They were calculated based on the available voltage and the desired trajectory. As the back emf of the machine changes during transition, the target voltages need to be adapted at each control interval to maintain the desired control trajectory. Thereby the available voltages in d-and q-direction vary, as the machine rotates electrically by 18 °. Figure 6 c) shows the time course of the flux linkages. Representing a straight line in the flux domain as described in chapter III. B).
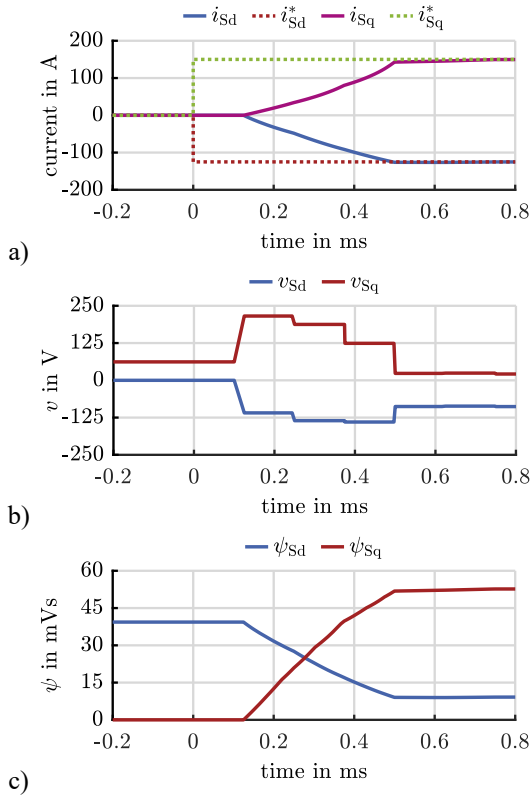

a)

b)

c)

Fig. 6. Time series of the setup at setpoint step at the PMSM.

B. synchronous reluctance machines

The data set for the simulation of the SyRM was created with the open source development platform *SyR-e Drive* that relies on *FEMM* and *MATLAB* [13]. The machine data is given in table II.

TABLE II. SYRM MACHINE DATA

Symbol	Meaning	value
p	Number of polepairs	3
i_{max}	Maximum rms stator current	35.4 A
v_{DC}	DC link voltage	565 V
P_{max}	Maximum power	10 kW
R_{S}	Stator resistance	44 mΩ

The flux maps in fig. 7 show that saturation and cross coupling is also present for this machine. Compared to the PMSM, the flux linkages of the SyRM are basically shifted by the permanent magnet flux, which corresponds to the machine model described in section II.
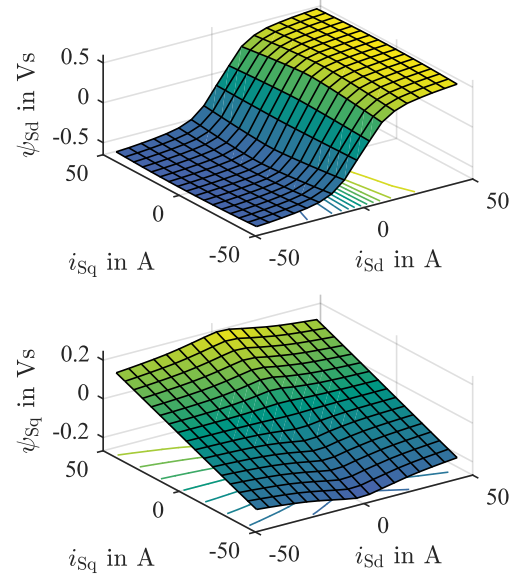

Fig. 7. Maps of the Sd- and Sq-flux linkage of the SRM DUT.

The setpoint step shown in fig. 8 is performed at 1500 rpm. The setpoint current was chosen to $i_{\text{Sd}} = -25$ A and $i_{\text{Sq}} = 43$ A. The controller reaches the new setpoint within 2 ms, which corresponds to 16 controller intervals. Fig. 8 b) shows the trajectory in flux domain. As exected, the identified flux linkages follow the defined target trajectory and representing a straight line in flux domain. In current domain (Fig. 8 a)) the course of the current is caused by the non-linearities represented by the flux maps. As expected, the current therefore doesn't follow a straight line to the new setpoint.
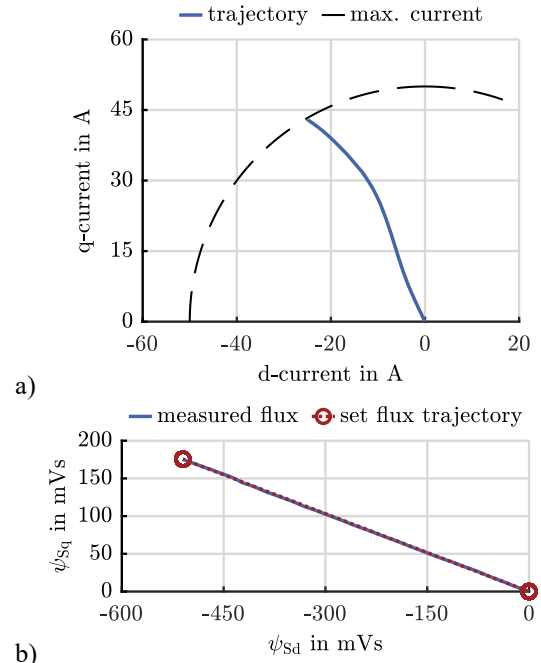

a)

b)

Fig. 8. Setpoint step at SyRM operation in current and flux domain.

V. Experimental Results

In this chapter, the experimental results for the EESM and IM are shown. In each case, the machine test stands are briefly introduced, followed by measurements.

A. Electrically excited synchronous machine

The test stand of the EESM is controlled by the *ETI-SoC-System* based on a *Xilinx XC7Z030* from the SoC family *Zynq-7000* using *MATLAB®* code generation [14]. The test bench shown in fig.9 consists of the *LTI LSH-127-4-30-560/T4,1R* PMSM load machine, which is speed controlled using a cascaded PI-control.

Fig. 9. Testbench with *LTI - LSH-127-4-30-560/T4,1R* (left) as load machine and the EESM DUT on the right.

The stator of the EESM DUT is driven by driven by a 3-phase-2-Level-IGBT-inverter (*ETI-combi-EPSR* [15]). The rotor is connected to two phases of a second *ETI-combi-EPSR* by slip rings. This allows full bridge operation with positive and negative rotor voltages.

Fig. 10 shows the flux maps of the DUT identified by measurements. A clearly nonlinear behavior of the machine at higher currents is evident. Compared to typical traction drives the inductances are high, resulting in reduced dynamics of the DUT.

The measurements shown in fig 11. where performed with the DC-link of rotor and stator power converter connected to the same source set to 100 V. This exceeds the nominal voltage of the rotor circuit given in table III and results in increased dynamics. The switching frequency equals the controller frequency and was set to 10 kHz. The rotational speed was set to 200 rpm. In fig. 11, a setpoint step is performed.

TABLE III. EESM MACHINE DATA [6]

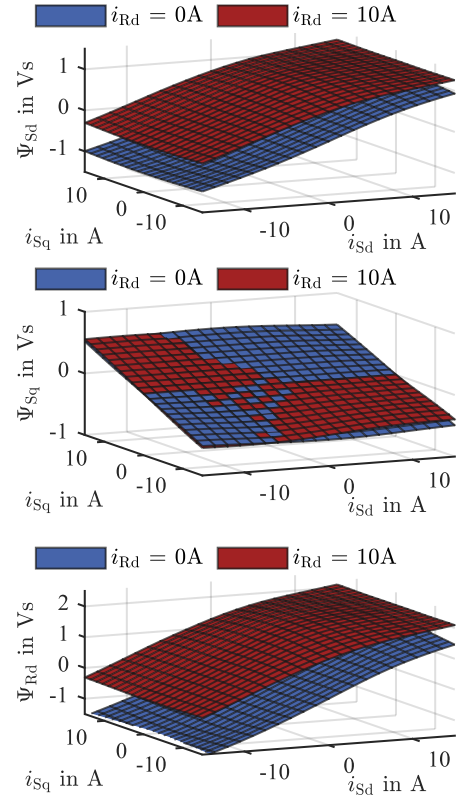| Symbol	Meaning	value
p	Number of polepairs	2
$i_{S,max}$	Maximum rms stator current	10.1 A
$i_{S,max}$	Maximum rms stator current	13 A
$v_{S,DC}$	Nominal stator DC link voltage	400 V
$v_{R,DC}$	Nominal rotor DC link voltage	48 V
$P_{cont.}$	Continuous Power	5.9 kW
R_S	Stator resistance	0.94 Ω
R_R	Rotor resistance	1.26 Ω

Fig. 10. Maps of the Sd-, Sq- and Se-flux linkage of the EESM DUT.

Fig. 11 a) shows the current response. The nonlinear machine behavior is present especially at the d-current resulting in a nonlinear current increase especially of i_{Sd}. The flux linkages shown in fig. 11 b) thereby follow the target trajectory given as straight line.
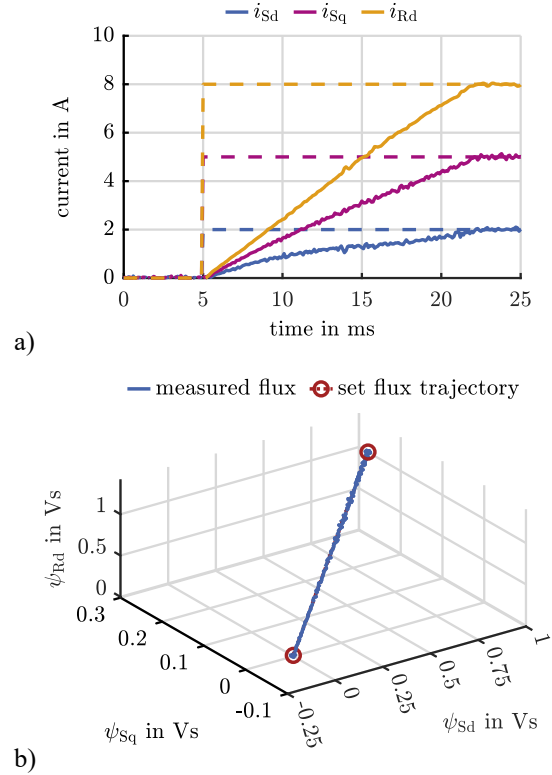
a)

b)

Fig. 11. Setpoint step at EESM operation in current domain (set value – dashed line) and flux domain.
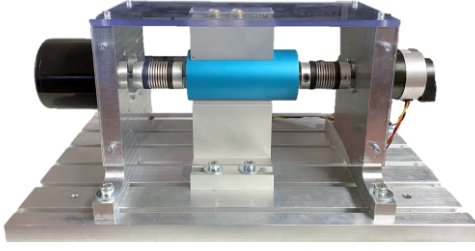
B. Induction motor

Fig. 12. Testbench with *Nanotec - DB59M024035R-B3* (right) as load machine and the *EM synergy M800006* as IM DUT (left).

The IM test bench shown in fig. 12 consists of a *Nanotec - DB59M024035R-B3* PMSM load machine and the *EM synergy M800006* DUT. It is driven by the power converter presented in [16]. The load machine is speed controlled using a cascaded PI-control. Control and monitoring of the test stand are performed by the *ETI-SoC-System* described in the previous chapter.
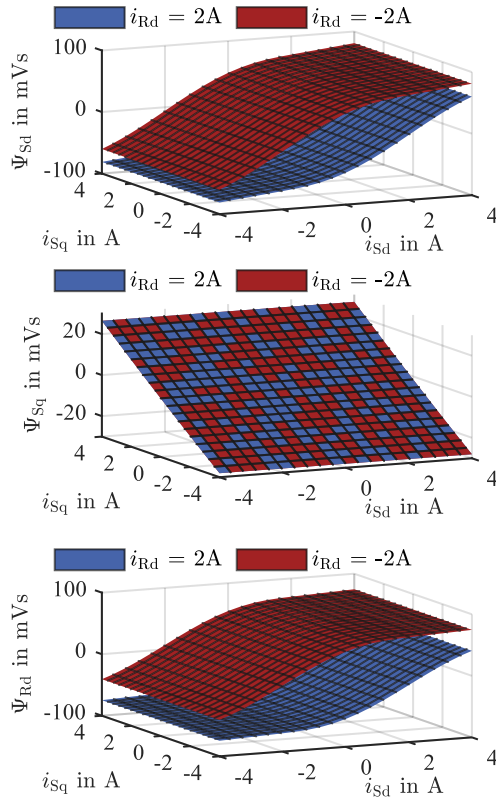

Fig. 13. Maps of the Sd-, Sq- and Se-flux linkage of the IM DUT.

Fig. 13 shows the flux maps of the DUT. They were identified by measurements according to [4]. To allow transient operation outside the identified area, the data was fitted and extrapolated. The IM also shows a clearly nonlinear behavior at high current amplitudes. Further machine data is given in table IV. It was determined in consultation with the manufacturer and additional measurements, as it exceeds the official data sheet values given in [17].

Fig. 14 shows the measurements on the test bench at 24 V DC-link voltage, 8 kHz switching frequency and 300 rpm at IM operation during 3 setpoint steps. The current limit was set to 3 A.

TABLE IV. SCIM MACHINE DATA

Symbol	Meaning	value
p	Number of polepairs	2
i_{max}	Maximum rms stator current	2.9 A
U_{DC}	DC link voltage	24 V
P_{max}	Maximum power	30 W
R_S	Stator resistance	1.13 Ω
R_R	Rotor resistance	0.9 Ω

Thereby, each current setpoint $\vec{\imath}^* = [i_{Sd}^*, i_{Sq}^*, i_{Rd}^* = 0]$ equals a point in the flux domain $\vec{\psi}^* = [\psi_{Sd}^*, \psi_{Sq}^*, \psi_{Rd}^*]$, which is reached in a straight line (Fig. 14 c). As the set trajectory in the flux domain is only executed as a projection in the d- and q-dimension, the rotor flux ψ_{Rd} deviates from the set trajectory. As expected, no deviations are present in the d- and q-dimensions. The rather simple trajectory in flux domain represents a complex trajectory in current domain (fig. 14 b) resulting in increased dynamics. The time course is shown in fig 14. a).
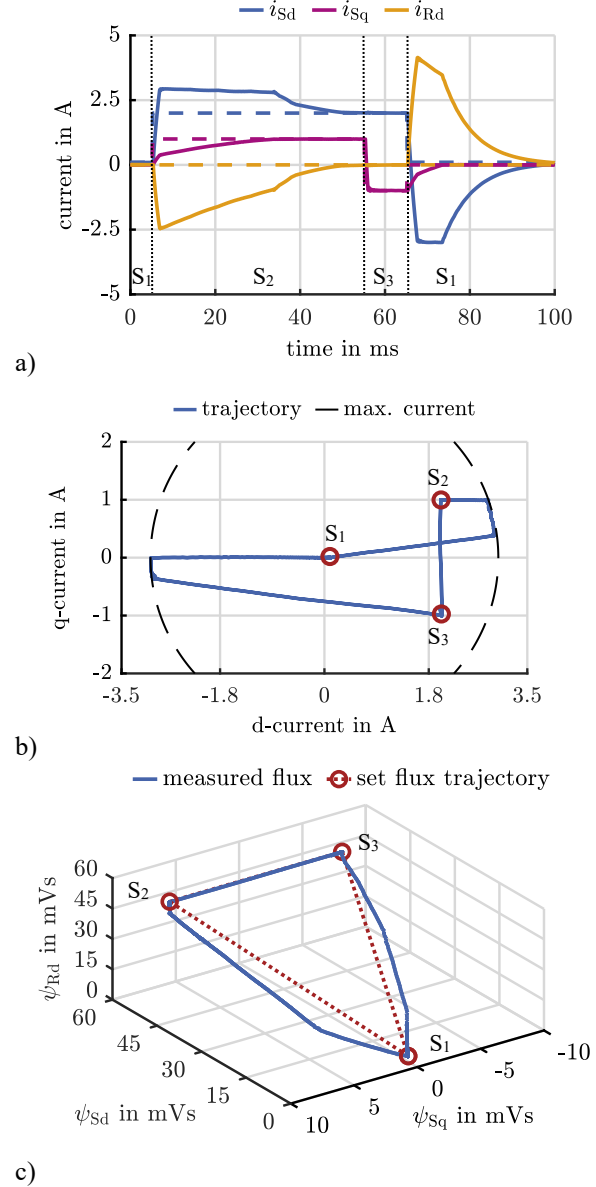

a)

b)

c)

Fig. 14. Setpoint step at IM operation in current and flux domain.

At $t = 5$ ms, the setpoint of i_{Sd} was changed from 0.1 A to 2 A and at i_{Sq} from 0 A to 1 A. Therefore, i_{Sd} is first raised up to the current limit of 3 A to increase ψ_{Rd} (fig. 14 b). After reaching the new setpoint, the currents remain constant. The next setpoint step of i_{Sq} to -1 A occurs at $t = 55$ ms. Since no adjustment of ψ_{Rd} is needed to reach the new setpoint, the settling time is significantly shortened as only i_{Sq} is adjusted. The last setpoint step to the initial values is performed at $t = 65$ ms. To decrease the rotor flux i_{Sd} is set to the current limit of -3 A (fig. 14. b). This allows performing all setpoint steps within 90 ms enabling dynamic control of the induction machine without constant rotor flux.

VI. Conclusion

In this paper, a new method for the unified nonlinear modelling and control of EESM, IM, PMSM and SyRM is presented. The results are based on extensive simulations and measurements. Accurate operation and the real-time capability of the algorithm have been demonstrated on different machine types in various power ranges. The results demonstrate the high dynamics of the new control algorithm despite its universal implementation.

As the presented algorithm is a P-controller, model errors lead to deviations. Therefore, precise data is crucial for accurate operation. Additional strategies will also be subject of future research.

VII. References

[1] S. Krüner and C. Hackl, "Experimental Identification of the Optimal Current Vectors for a Permanent-Magnet Synchronous Machine in Wave Energy Converters," *Energies*, vol. 12, no. 5, p. 862, 2019, doi: 10.3390/en12050862.

[2] J. Kullick and C. M. Hackl, "Generic machine identification and maximum efficiency operation of induction machines," Dec. 2018. [Online]. Available: https://arxiv.org/pdf/1812.02431

[3] J. Tang and Y. Liu, "Design and Experimental Verification of a 48 V 20 kW Electrically Excited Synchronous Machine for Mild Hybrid Vehicles," in pp. 649–655.

[4] Johannes Stoss, Akif Karayel, Leonard Geier, Andreas Liske, Marc Hiller, "Identification of rotor and stator flux linkage maps of squirrel cage induction motors based on identification of rotor time constant maps," *2023 25rd European Conference 2023*, vol. 2023.

[5] J. Richter and M. Doppelbauer, "Predictive Trajectory Control of Permanent-Magnet Synchronous Machines With Nonlinear Magnetics," *IEEE Trans. Ind. Electron.*, vol. 63, no. 6, pp. 3915–3924, 2016, doi: 10.1109/TIE.2016.2527628.

[6] Patrick Winzer, Jan Richter, and Martin Doppelbauer, "Dynamic Control of Generalized Electrically Excited Synchronous Machines Using Predictive Flux Control," 2016.

[7] J. Richter, A. Dollinger, and M. Doppelbauer, "Iron loss and parameter measurement of permanent magnet synchronous machines," in *2014 International Conference on Electrical Machines (ICEM 2014): Berlin, Germany, 2 - 5 September 2014 ; [proceedings*, Berlin, Germany, 2014, pp. 1635–1641.

[8] L. Tolosano, E. Armando, S. Rubino, F. Mandrile, and R. Bojoi, "Experimental Identification of Induction Machine Flux Maps for Traction Applications," in *2022 IEEE Energy Conversion Congress and Exposition (ECCE)*, Detroit, MI, USA, Oct. 2022 - Oct. 2022, pp. 1–8.

[9] Patrick Winzer, "Steigerung von Drehmoment und Wirkungsgrad bei Synchronmaschinen durch Nutzung der magnetischen Asymmetrie," 2017.

[10] Leonard Geier, Johannes Stoss, Andreas Liske, Marc Hiller, "Generalized Inversion of n-dimensional Flux Maps for Unified Nonlinear Machine Models and Predictive Control Algorithms," *2023 IEEE Energy Conversion Congress*.

[11] J. Richter, P. Winzer, and M. Doppelbauer, "Einsatz virtueller Prototypen bei der akausalen Modellierung und Simulation von permanenterregten Synchronmaschinen. Application of virtual prototypes of permanent magnet synchronous machines by acausal modeling and simulation," 2013.

[12] M. Schiefer, "Indirekte Wicklungskühlung hochausgenutzter permanenterregter Synchronmaschinen mit Zahnspulenwicklung," Dissertation, Karlsruher Instituts für Technologie (KIT). [Online]. Available: https://publikationen.bibliothek.kit.edu/1000076110

[13] A. Varatharajan, D. Brunelli, S. Ferrari, P. Pescetto, and G. Pellegrino, "syreDrive: Automated Sensorless Control Code Generation for Synchronous Reluctance Motor Drives," in *2021 IEEE Workshop on Electrical Machines Design, Control and Diagnosis (WEMDCD)*, 2021, pp. 192–197.

[14] B. Schmitz-Rode *et al.,* "A modular signal processing platform for grid and motor control, HIL and PHIL applications," in *IPEC 2022 ECCE Asia Himeji: International Power Electronics Conference : May 15-19, 2022, Himeji City Culture and Convention Center*, Himeji, Japan, 2022, pp. 1817–1824.

[15] R. Schwendemann, S. Decker, M. Hiller, and M. Braun, "A Modular Converter- and Signal-Processing-Platform for Academic Research in the Field of Power Electronics," in *2018 International Power Electronics Conference (IPEC-Niigata 2018 - ECCE Asia)*, 2018, pp. 3074–3080.

[16] J. Stoß, C. Wurster, N. Menger, M. Brodatzki, A. Liske, and M. Hiller, "Design guideline for PCB integrated, high bandwidth, current slope sensing based on a planar Rogowski coil," in *2021 23rd European Conference on Power Electronics and Applications (EPE'21 ECCE Europe)*, 2021, P.1-P.10.

[17] Texas Instruments and EMsynergy, *Datasheet: Low Voltage AC Induction Motor*. [Online]. Available: https://www.ti.com/lit/ug/spruhz8/spruhz8.pdf?ts= 1654676761586 (accessed: Jun. 8 2022).